ROYAL SOCIETY
OF CHEMISTRY

PAPER

Check for updates

Assembly of small silica nanoparticles using lipid-tethered DNA 'bonds'

Huat Thart Chiang, [ID] [a] Naomi Kern,[a] Zachery R. Wylie, [ID] [a] Abdul Moeez,[b] Haoqing Zhang,[a] Daniel McKeen,[c] Nicholas S. M. Herringer,[f] Oleg Gang,[cde] Andrew L. Ferguson, [ID] [fg] Zachary Sherman [ID] [a] and Lilo D. Pozzo [ID] ⋆[ab]

Single-stranded DNA molecules modified with cholesterol functional groups are physically tethered to silica nanoparticles (diameter 25 nm) that are encapsulated in a lipid bilayer. Such tethering increases the azimuthal mobility of the DNA molecules across the nanoparticle surface and enables nonspecific bonding, eliminating the need for specialized surface chemistries (such as silane or thiol ligands). To induce assembly, double-stranded DNA 'bridge' molecules are then added with complementary nucleotides to the DNA 'anchor' molecules that are physically tethered to the lipids on the surface of the particles. Assembly is observed to occur at room temperature and without the need for temperature annealing. Using automated liquid handling tools, assemblies are created in high throughput and rapidly characterized using SAXS. It is determined that the relative concentration of DNA-to-silica and the ionic strength of the solution are important parameters that affect the resulting assembly. Analysis of SAXS data is performed using coarse-grained particle dynamics simulations. The results support the spontaneous formation of semi-crystalline particle assemblies by particle condensation, where the interparticle distance is tuned by the sequence of the DNA 'bridge' used to link the particles. Crystallinity analysis performed on the resulting simulations, optimized to match SAXS observations, suggest that particle clusters display increased crystallinity in the center of the clusters, but their maximum size remains relatively small (sub-micron) before settling occurs, which limits the extent of crystallization.

Introduction

DNA-mediated assembly has emerged as a powerful strategy for organizing colloidal particles into ordered structures, owing to the highly specific and programmable interactions inherent to DNA molecules.[1,2] DNA's specificity arises from its nucleotide sequence-specific complementary base paring. DNA's programmability arises from the vast number of possible nucleotide base pair combinations, which can be engineered to precisely control key parameters such as strand length and melting temperature. In the literature, the most established and common approach utilizes single-stranded DNA molecules functionalized with thiol groups to chemically bind to gold nanoparticles. These DNA functionalized nanoparticles can then be programmed with 'sticky ends' which are short, single-stranded DNA molecules designed to hybridize selectively with complementary sequences on neighboring particles. After thermal annealing, which involves heating the DNA-functionalized particles to a monomeric state beyond the DNA melting temperature, followed by controlled slow cooling, these sticky ends reversibly hybridize, leading to the reorganization of nanoparticles into highly ordered crystal superlattices, as demonstrated in several foundational studies.[3,4]

While gold–thiol chemistry is a well-established method for anchoring DNA to nanoparticle surfaces, the resulting covalent bonds render the DNA immobile. This rigidity can potentially hinder structural rearrangements during the assembly process. In contrast, anchoring DNA–cholesterol conjugates within a fluid lipid bilayer *via* hydrophobic interactions offers an alternative strategy, which has also been well documented in the literature but for micron-sized colloids.[5–7] The bilayer's inherent fluidity allows DNA strands to diffuse azimuthally across the nanoparticle surface, enabling real-time reconfiguration of interparticle connections and potentially enhancing the formation of

[a] *Department of Chemical Engineering, University of Washington, Seattle, WA 98195, USA. E-mail: dpozzo@uw.edu*

[b] *Molecular Engineering and Sciences Institute, University of Washington, Seattle, WA 98195, USA*

[c] *Departments of Chemical Engineering and Applied Physics and Mathematics, Columbia University, New York, NY 10027, USA*

[d] *Center for Functional Nanomaterials, Brookhaven National Laboratory, Upton, NY, 11973, USA*

[e] *Center for Nanomedicine, Institute for Basic Science (IBS), Seoul, 03722, Republic of Korea*

[f] *Department of Chemistry, University of Chicago, Chicago, IL, 60637, USA*

[g] *Pritzker School of Molecular Engineering, University of Chicago, Chicago, IL 60637, USA*

ordered superlattices. Given this difference in surface dynamics, it is important to assess the functional impact of fluid bilayers in the context of DNA-mediated nanoparticle assembly. In this work, we investigate how this mode of DNA attachment compares to conventional gold-thiol systems in assembling three-dimensional colloidal superlattices.[8]

There are several possible advantages of DNA surface mobility in forming colloidal superlattices. For example, DNA shell flexibility at the nanoscale has been increasingly recognized as a crucial factor in promoting well-defined crystal formation.[3,9] In our system, the expected increase in azimuthal mobility of DNA on fluid-supported nanoparticles introduces an added degree of freedom that enables the particles to adjust their positions relative to one another. This dynamic behavior could facilitate assembly by helping the system escape kinetic traps and resolve local defects that would otherwise stall the assembly process.[5] Furthermore, particle dynamics simulations have demonstrated that bond mobility can give rise to a rich variety of assembled structures such as aperiodic arrangements, shape-diverse tilings, and open porous frameworks that are typically inaccessible in systems with fixed DNA linkers.[10] Despite these insights, experimental investigations into mobile DNA bonds on nanoparticles remain scarce. This work begins to address this gap by exploring how physically-bound DNA with increased surface mobility influences the assembly dynamics and structural outcomes of DNA-programmed colloidal assembly at the nanoscale.

Materials and methods

Chemicals

LUDOX TM-50 colloidal silica (50% weight) and sodium chloride ($\geq$99%) were purchased from Sigma Aldrich (St. Louis, MO, USA) and used as received. 1,2-Dioleoyl-*sn-glycero*-3-phospho-choline (DOPC) ($\geq$99%) was purchased from Avanti Polar Lipids (Alabaster, Alabama) and used as received. Deionized water was obtained from a Direct-Q 3 UV water purification system with a resistivity of 18.2 MΩ (Millipore Corporation, Bedford, MA, USA).

DNA

All DNA was ordered from Integrated DNA Technologies (IDT) (Coralville, IA, USA). Further details such as the sequences can be found in the SI.

Dynamic light scattering

DLS measurements were taken on a Malvern PANalytical (Malvern, United Kingdom) Zetasizer Nano ZS in a polystyrene cuvette.[11,12] The wavelength of the laser was 633 nm. The refractive index of Silica and lipids was assumed to be 1.44[13,14] and that of the water solvent was 1.33. To analyze the data, the General Purpose algorithm provided by the Zetasizer software was used, which performs cumulant and CONTIN analyses of the autocorrelation function (ACF). The hydrodynamic diameter was determined from the intensity-weighted particle size distribution.

Small angle X-ray scattering

Experimental SAXS data was obtained on a Xenocs Xeuss 3.0 (Grenoble, France) instrument with an X-ray energy of 8.04 keV (wavelength 1.54 Å) using a copper K-α microfocus source. Data was collected in two configurations: low-q (0.003–0.007 Å^{-1}) using the ESAXS standard setting for 1200 s and mid-q (0.007–0.10 Å^{-1}) for 600 s using the SAXS high intensity setting. The samples had a volume of 200 μL and were created in a specially designed wellplate with 48 wells. The wellplate was designed so that it would collect any sedimentation from samples in a small pocket at the bottom of the wells. The X-ray beam can then be positioned on this small pocket to obtain the scattering curve of the sediment. Design files to create the wellplate can be found on (Github). Background reduction was performed with the XSCAT software by subtracting the scattering of water in the same wellplate and the data was merged automatically using a Python code.

Small angle neutron scattering

Experimental SANS data were obtained on the Bio-SANS instrument at the High Flux Isotope Reactor at Oak Ridge National Laboratory. Samples were placed in a 2 mm thick Hellma (Banjo) cell with a volume of 600 μL, and a sample exposure time of 1 hour was used. A dual detector system composed of a curved wing detector at 1.13 m and a flat main detector at 15.5 m provided a continuous range of momentum transfer values q from (0.003–0.8 Å^{-1}). The neutron wavelength (λ) was 6 Å with a distribution (dl/l) of 13.2%. Data reduction was performed with the DRTSANS reduction software provided by the facility.

Electron microscopy

Scanning electron microscopy and energy dispersive spectroscopy (SEM-EDS) were performed on samples using a Thermo Fischer Phenom Pharos G2 SEM-STEM. Samples were prepared by the drop casting of diluted nanoparticles onto carbon film, 200 mesh nickel grids (Electron Microscopy Sciences; Hatfield, PA). Grids were placed onto a circular piece of filter paper, carbon side up, and 10 μL of the dilute suspension was dropped onto the grid and allowed to dry.

Liquid handling

The pipetting to mix samples in the wellplate for SAXS characterization was performed by an Opentrons (Brooklyn, NY, USA) OT2 liquid handling robot. The OT2 control code can be found on (Github).

Sonication

Sonication was performed with a Branson 450 digital sonifier using a probe of 3/4″ diameter. Samples were sonicated in 20 mL scintillation vials for 1 minute at a power of 10% with a pulse interval of 10 s (5 s on/off). Immediately after this first sonication, they were resonicated for 5 minutes at a power of 30% with a pulse interval of 10 s (5 s on/off). To determine the delivered power, a calorimetric measurement was performed by

measuring the change in temperature of 10 mL of deionized water under the sonication settings. For the setting with 10% amplitude, the delivered power was 10 Watts, and for the setting of 30% amplitude, the delivered power was 29 Watts.

Lipid encapsulation with DOPC

To encapsulate the silica nanoparticles in a lipid bilayer, the total surface area of the nanoparticles was first calculated. Based on this calculation, the required amount of DOPC to completely coat their surface was determined. The first step was to create a silica nanoparticle stock suspension of 60 mg mL^{-1} silica nanoparticles in water using the Ludox TM-50 product, which has a silica weight percent of 50. A DOPC stock solution was also created containing 50 mg mL^{-1} DOPC in chloroform. The sample of silica nanoparticles encapsulated in DOPC was created in a 20 mL scintillation vial. First, 142 μL of the 50 mg mL^{-1} DOPC stock solution (7 mg of DOPC) was added to the vial. The uncapped vial was placed in a vacuum oven under vacuum at room temperature for an hour in order for the chloroform to evaporate. After this, 333 μL of the 60 mg mL^{-1} silica stock suspension (20 mg of silica) was added as well as 9666 μL of deionized water. The final step was to sonicate the sample using the sonicator horn with the settings described in the sonication section.

Particle simulations

Particle dynamics simulations were performed using HOOMD-blue (v2.9.4)[15] to model the self-assembly of DNA-functionalized nanoparticles under Langevin dynamics. The simulation setup closely follows the implicit interaction model described by Mao *et al.*,[16] in which DNA-mediated attractions are represented as short-range isotropic pair potentials between spherical particles. In their work, the pair potentials are validated using the potential of mean force calculated from a more realistic coarse-grained simulation of the DNA-mediated assembly of nanoparticles. Our simulations consisted of $N = 5000$ spherical particles of diameter $\sigma = 1.0$, randomly distributed in a cubic simulation box with periodic boundary conditions. The box length L was computed based on the target number density $\rho = N/V$, with the initial configuration generated by randomly placing particles with a minimum center-to-center distance of 1.1σ to prevent overlaps. The interparticle interactions were modeled using a modified Lennard-Jones potential of the form:

$$U(r) = \frac{U_0}{n - m}\left[m\left(\frac{r_0}{r}\right)^n - n\left(\frac{r_0}{r}\right)^m\right] \tag{1}$$

where U_0 is the interaction strength in units of kT, r is the interaction distance in units of σ, r_0 is the distance where the interaction is minimum in units of σ, and n and m define the 'steepness' of the repulsive and attractive components, respectively. The potential was tabulated between $r_{min} = 0.75r_0$ and $r_{max} = 5.0$ using 1000 linearly spaced points and implemented *via* HOOMD's pair.table module. All potential values were pre-validated to avoid non-finite values that could disrupt force evaluations. The system was simulated under

Langevin dynamics using a time step $\Delta t = 0.001$ (reduced units), equal to around 18 picoseconds, and thermal energy $k_B T = 1.0$. Simulations were run for 1.5×10^7 time steps. System snapshots were recorded every 1000 steps using GSD (general simulation data) trajectory output. In addition, the potential energy of the system was visualized and saved to confirm that the system reached a state close to equilibrium.

Simulated scattering curves were calculated from particle configurations of the last six saved snapshots of the simulation evenly spaced apart by 50 000 timesteps using a Monte Carlo sampling of the Debye equation,[17] and averaged to obtain a single simulated scattering curve of the system at a state close to equilibrium. The simulated curve was converted into a structure factor and compared to the experimental structure factor using the Amplitude-phase similarity metric[18] to obtain a similarity score. The score was then used to inform a Bayesian optimization algorithm (botorch v0.10.0)[19] on simulation parameters for the next iteration. A total of 100 iterations were run for each optimization and each iteration took around 15 minutes to run. Computations were executed on a single gpu-l40 node equipped with 32 Intel CPU cores, 96 GB RAM, and one NVIDIA L40 GPU (48 GB GDDR6).

Results and discussion

Overview of assembly strategy

The method presented in this work to assemble silica nanoparticles involves first encapsulating them in a lipid bilayer composed of DOPC. Next, single-stranded DNA modified with a cholesterol molecule on the 3′ end (DNA–Chol) is added to the system. The cholesterol embeds itself into the bilayer due to hydrophobic interactions, while the DNA forms a corona on the lipid bilayer. Because the lipids used are unsaturated, the bilayer is expected to be fluid at room temperature, allowing for DNA mobility on the surface of the bilayer. To induce assembly, a double-stranded DNA molecule (DNA-Bridge) is added. The double-stranded DNA has single-stranded sticky ends on each side which are complementary to the single-stranded DNA–Chol molecule previously embedded into the bilayer. A schematic of this process is shown in in Fig. 1. More detailed discussions on the choice of nanoparticles, lipids, and DNA sequences are presented in the following sections.

Choice of nanoparticle

Using the method described in this work, it should be possible to assemble many different types of nanoparticles of variable shape, size, and composition, provided that they can be encapsulated within the lipid bilayer structure. To demonstrate this concept, we chose to assemble low polydispersity silica nanoparticles of 25 nm in diameter. This material was chosen for several reasons. The first reason is that there is high electron density contrast between silica and water, which facilitates SAXS measurements on the assembled structure, and there is also good availability at high particle concentrations, variable particle sizes, and with low polydispersity. This contrasts to
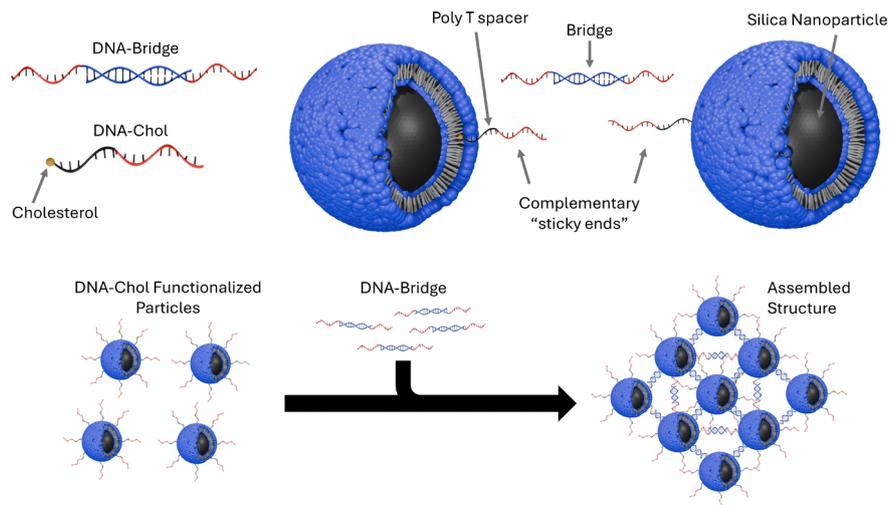
Fig. 1 The DNA design used to assemble the silica particles (figure not drawn to scale). DNA–Chol is first added to functionalize the particles, followed by a premixed DNA-Bridge that links two DNA–Chol strands together. DNA-Bridge can be inexpensively tuned to test different lengths or binding energies on the assembly.

traditionally used gold nanoparticles, where typical particle concentrations are many orders of magnitude lower. A second reason is that low polydispersity silica nanoparticles can be inexpensively synthesized using the Stöber method.[20] Low polydispersity is essential for the formation of crystals since disorder can propagate and result in a loss of periodicity. Ludox-TM50 meets these requirements and is selected for this experiment.

Choice of lipid

Several criteria must be met to select the appropriate lipid for assembling the silica nanoparticles. The first criterion is that the lipid must be able to encapsulate the nanoparticles with a bilayer. This means that the lipid heads must have a strong adsorption affinity to negatively charged silica nanoparticles. The second criterion is that the lipids must not be cationic which would cause the adsorption of negatively charged DNA molecules on the surface of the bilayer, preventing them from being used to induce assembly. Finally, to achieve assembly without thermal annealing, the lipid must have a low melting point to allow for a fluid bilayer to form. A lipid that satisfies all criteria is DOPC, which is chosen as the primary lipid in this work. DOPC has a critical packing parameter (CPP) of about 0.66 which results in lamellar self-assembled structures.[21] Despite being zwitterionic, it has a strong affinity towards silica nanoparticles, which is well reported in the literature,[22–24] and hypothesized to originate from hydrogen bonding, ion–dipole, dipole–dipole, and van der Waals interactions.[25] It is also unsaturated, with a gel phase melting point of -20 °C.[26] Thus, it was hypothesized that a fluid bilayer would form at room temperature, allowing for increased mobility of the 'anchored' DNA on the surface.

DNA sequence

The DNA sequence is also crucial for forming the desired type of crystal. Factors such as the 'sticky end' binding energy and the total length of nucleotides are common design variables. In this work, we first functionalize the lipid-encapsulated silica nanoparticles with single-stranded DNA which is modified with a cholesterol molecule on the 3′ end (referred to as DNA–Chol). Separately, two single-stranded DNA molecules are designed and mixed to hybridize, forming a DNA 'bridge' with double-stranded DNA in the center with unhybridized single-stranded ends (referred to as DNA-Bridge). These single-stranded ends are complementary to the 'sticky ends' from the DNA–Chol, which is used to functionalize the nanoparticles. Assembly is then induced by adding DNA-Bridge to the nanoparticles functionalized with DNA–Chol. One advantage of this strategy is that assembly can be triggered simply by adding the DNA-Bridge. This allows for well-controlled experiments to compare the structures of the nanoparticle assemblies with and without the addition of the DNA-Bridge. Such comparisons would not be feasible in a strategy where nanoparticles are grafted with self-complementary DNA–Chol. The second advantage is that all DNA–Chol grafted nanoparticles are identical, making the formation of the crystal statistically more likely than if nanoparticles were individually grafted with two different complementary DNA–Chol strands and then mixed. The last advantage relates to the cost of DNA. DNA–Chol is considerably more expensive than DNA-Bridge due to the cholesterol modification. With this approach, we can test various bridge lengths and 'sticky end' base pairs by adjusting the sequence of the DNA-Bridge, which is more cost-effective and simpler than altering the sequence of two DNA–Chol molecules.

A final consideration for the DNA sequence is that the strand must be shorter than 50 nm, which corresponds to the persistence length of a double-stranded DNA molecule.[27] This ensures that the DNA-Bridge does not bind to DNA–Chol strands on the same nanoparticle. In our experiments, the DNA length separating the particles is well below the persistence length, so the DNA

behaves as a stiff rod, making intraparticle binding highly unlikely.

Lipid encapsulation of silica nanoparticles

The initial step to assemble nanoparticles with lipids and DNA involved encapsulating the nanoparticles within a lipid bilayer, as detailed in the Methods section. To test if this structure was actually formed, a control sample consisting of silica nanoparticles of the same concentration (2 mg mL^{-1}) without any DOPC was also created. The two samples were characterized using dynamic light scattering (DLS), amall-angle neutron scattering (SANS), and small-angle X-ray scattering (SAXS).

Small angle scattering techniques are useful to determine if the silica nanoparticles are successfully encapsulated in lipid bilayers because they are sensitive to structures over broad length scales and contrast can be manipulated to highlight different molecular components in composite systems. For example, information on the diameter of a lipid vesicle, as well as the thickness of the bilayer, can be obtained from small angle scattering. The main difference between SAXS and SANS is the contrast of silica and DOPC with the suspending solvent. SAXS is more sensitive to silica than to lipids due to the higher X-ray contrast (*i.e.* electron density) between silica and water *versus* lipids and water. Because of this, the scattering curves of bare silica nanoparticles and those of encapsulated particles are expected to resemble spherical particles with low polydispersity. On the other hand, using contrast variation neutron scattering, high neutron contrasts of both lipids and silica can be obtained in a solvent of high D$_2$O content, meaning that the scattering curve would have contributions from both materials. The solvent composition for the SANS samples was chosen to be 89% D$_2$O. The solvent composition for the SANS samples was chosen to be 89% D$_2$O. This reduces the contribution of incoherent scattering, which results in a lower background in the SANS measurements and improves data quality. The experiments were not performed in a fully enriched D$_2$O solvent

because the silica nanoparticle stock suspension was purchased in H$_2$O. To maintain nanoparticle stability, by avoiding dialysis or filtration into D$_2$O, a small amount of H$_2$O had to be retained in the sample dispersion. SAXS and SANS characterization were performed on the two silica samples, one with and one without DOPC. The scattering curves are shown in Fig. 2.

Fig. 2(A) demonstrates that the SAXS intensity as a function of wavevector transfer, $I(q)$, for the two silica samples with and without DOPC are comparable. The spherical model used to analyze the data fits the data well, demonstrated by the good alignment between the data and the model. From the fit, a sphere diameter of 25 nm with a polydispersity index of 0.11 was obtained. The SAXS profile of the sample containing silica and DOPC is also plotted in Fig. 2(A) and closely resembles the data of the sample without any lipid. This can be explained because lipids do not significantly alter the scattering signature due to their low X-ray contrast with respect to water. The slight increase in the power-law slope at low q may be attributed to minor nanoparticle aggregation or to the presence of some larger DOPC vesicles in solution. Fig. 2(B) shows the SANS data of the two samples along with the models used to fit the data. As expected, there are major differences between the two SANS curves due to the high neutron contrast of the lipids with the D$_2$O enriched solvent. To model the data of bare silica, a sphere model was used and a diameter of 24.6 nm with a polydispersity index of 0.15 was obtained which is similar to the values independently obtained from SAXS. To model the data of the sample containing silica nanoparticles with DOPC, a model composed of the sum of two core–shell spheres was used. The first core shell sphere represents the silica nanoparticles encapsulated in a lipid bilayer and the second core shell sphere represents large free vesicles. This was done by assigning the appropriate scattering length densities to each material as shown in Fig. 3. The parameters describing the size of the silica nanoparticle inside the lipid bilayer were also fixed since they were determined from the sphere fit. From the fit of the
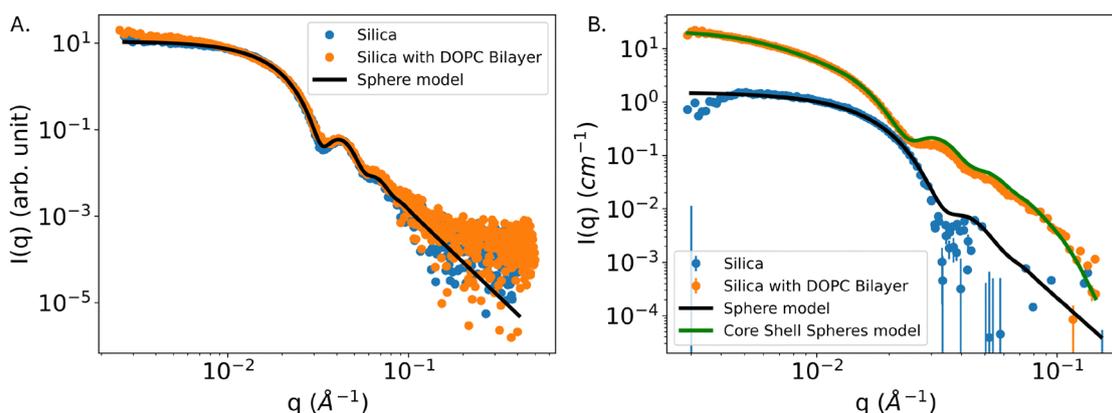

Fig. 2 Two samples were characterized with SAXS and SANS. The first sample contains a dispersion of (2 mg mL^{-1}) silica nanoparticles. The second sample contains a dispersion of (2 mg mL^{-1}) silica nanoparticles encapsulated with DOPC, which is prepared using the techniques discussed in the Methods section. (A) Shows the SAXS curves of the two samples along with a sphere model fit. Both samples were prepared in water. (B) Shows the SANS curves of the two samples along with a sphere model fit and a core shell sphere model fit. Both samples were prepared in 89% D$_2$O, which gives a high contrast for both the silica and lipids, and also reduces incoherent scattering from H$_2$O, improving data quality.
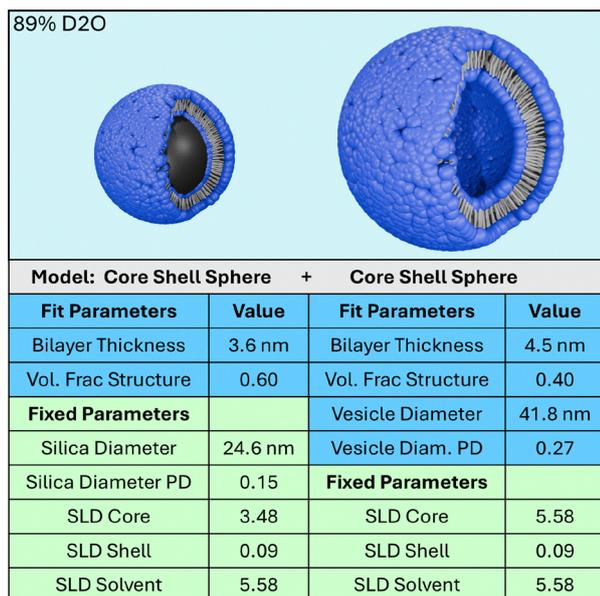
89% D2O

Model: Core Shell Sphere	+	Core Shell Sphere	
Fit Parameters	**Value**	**Fit Parameters**	**Value**
Bilayer Thickness	3.6 nm	Bilayer Thickness	4.5 nm
Vol. Frac Structure	0.60	Vol. Frac Structure	0.40
Fixed Parameters		Vesicle Diameter	41.8 nm
Silica Diameter	24.6 nm	Vesicle Diam. PD	0.27
Silica Diameter PD	0.15	**Fixed Parameters**	
SLD Core	3.48	SLD Core	5.58
SLD Shell	0.09	SLD Shell	0.09
SLD Solvent	5.58	SLD Solvent	5.58

Fig. 3 The hypothesized structure of the materials in the sample consisting of silica and DOPC. The table in the figure shows the parameters obtained from fitting the SANS data of the sample containing silica and DOPC. The values for the fixed parameters of the silica diameter and silica diameter polydispersity were obtained from fitting a sphere model to the sample that only contained silica. The values from the fit parameters were obtained from fitting the SANS data of the sample with silica and DOPC using a model consisting of the sum of two core shell sphere.[28] The units of the scattering length densities are ($\times 10^{-6}$ Å^{-2}). References for the scattering length densities can be found in the SI. The SasView application was used to fit the data.

sample containing silica and DOPC, additional structural parameters such as the thickness of the bilayer were obtained and are shown in Fig. 3.

The values from the fit show that the sample is consistent with silica nanoparticles encapsulated in a lipid bilayer of around 3.6 nm in thickness, which is close to the thickness of a lipid bilayer of POPC, a lipid with size and structure similar to DOPC, found in the literature.[29] This structure makes up the majority of the sample with a volume fraction of about 0.60. In addition to this structure, there are also vesicles in the solution that have a diameter of 41.8 nm and occupy a volume fraction of about 0.40. The thickness of the 'free vesicle' bilayer is 4.5 nm which slightly increased compared to when it was supported by the silica nanoparticle. This increase is also consistent with findings from the literature.[29] Overall, the scattering data from both SANS and SAXS is consistent with silica nanoparticles encapsulated with a DOPC bilayer.

In addition to small angle scattering, dynamic light scattering was also performed on the two samples. The hydrodynamic diameter of the sample with bare silica is around 32 nm and when the DOPC is added, it increases to about 60 nm. This increase in size is significantly more than the size increase that is expected due to a bilayer forming on the particles (7.2 nm). An explanation for this could be the presence of some larger vesicles in the sample determined by SANS, which were found to be around 42 nm in diameter with some polydispersity. It is

well known that the intensity-weighted analysis for DLS emphasizes the contribution of larger species, resulting in the larger average size. Moreover, DLS can also overestimate size when there is significant hydration of the interface that can reduce the expected diffusion coefficient of the particles.

High-throughput assembly screening

To rapidly explore the large experimental design space, automated robotic synthesis and SAXS characterization were used. Samples were composed of a mixture of silica nanoparticles encapsulated in a DOPC bilayer following the procedures from the previous section, DNA–Chol, NaCl and DNA-Bridge. Water was added to each sample to obtain a sample volume of 200 µL. The high-throughput experiment was designed to test different concentrations of DNA–Chol (20, 60, 100, 140 DNA Molecules per Particle) and NaCl (0, 10, 20, 30, 40 mM). The concentration of the DNA-Bridge was set so that there would always be one DNA-Bridge molecule for every two DNA–Chol molecules in the sample. The excess addition of the 'bridge' DNA construct could cap the particles and prevent them from binding. Controlled experiments were also performed where all samples were recreated with the same formulation, except for the addition of DNA-Bridge. The purpose of this was to confirm that assembly is induced by the addition of the DNA-Bridge and does not occur in its absence. The concentration of silica nanoparticles encapsulated in DOPC bilayers was kept constant at 1 mg mL^{-1} for all samples. Samples were prepared in a custom well plate designed to hold 48 samples. Each well features a small chamber at the bottom to collect the assemblies as they sediment due to gravity. This design enables precise positioning of the X-ray beam on the sediment for high-throughput SAXS characterization of the resulting assemblies. While the sample temperature can be adjusted by placing the well plate in an oven, SAXS measurements were limited to room temperature when using this well plate.

The results of the high-throughput screening experiment presented in Fig. 4 are summarized in Fig. 5, which shows the resulting SAXS data for the samples assembled at room temperature without any thermal annealing. The SAXS data for samples that were heated to 50 °C and slowly cooled to room temperature (i.e. thermally annealed) are almost identical and can be found in the SI. It was concluded that thermal annealing did not significantly affect the state of assembly under these conditions. Based on the SAXS profiles, three distinct structural regimes were identified and are highlighted in green, purple, and light blue. In the green region, the SAXS curves are characteristic of unassembeled, dispersed spherical particles. Notably, the similarity between the red and blue curves suggests that the presence of DNA-Bridge does not alter the sample structure in this regime. Since no NaCl is present in this region, these observations imply that some electrostatic screening is beneficial for particle assembly. One possible explanation is that addition of NaCl reduces electrostatic repulsion between anionic DNA–Chol strands adsorbed onto the lipid bilayer, or between DNA–Chol and the particle surface, thereby facilitating a higher density of DNA molecules on the surface.[30] It is
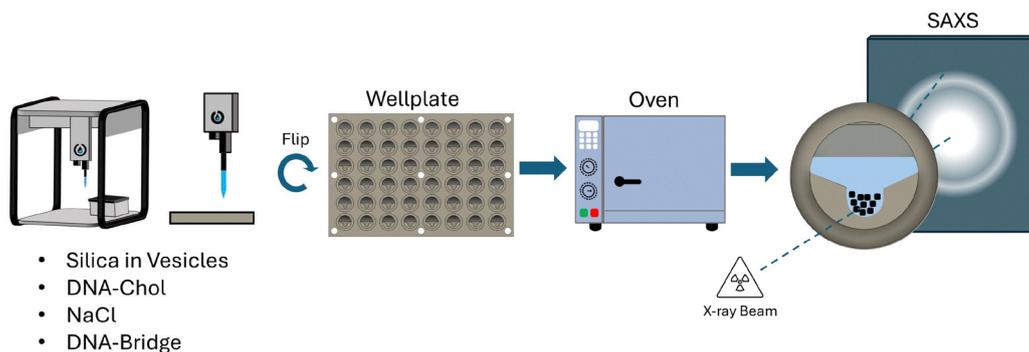
Fig. 4 The process used to screen the effect of NaCl and DNA–Chol concentrations on the assembly of DOPC encapsulated silica nanoparticles in high throughput. Samples were first mixed using a liquid handling robot in a custom wellplate. After sealing and flipping the wellplate in the upright position, any sediment from the sample accumulates in a small pocket in the bottom of the well, where the X-ray beam for SAXS can be positioned. To also assess the effects of thermal annealing, SAXS was measured both before heating the wellplate in an oven (not shown in the figure) and also after heating the wellplate to the melting point of the DNA in the oven and then cooling to room temperature. All SAXS data was taken at room temperature.
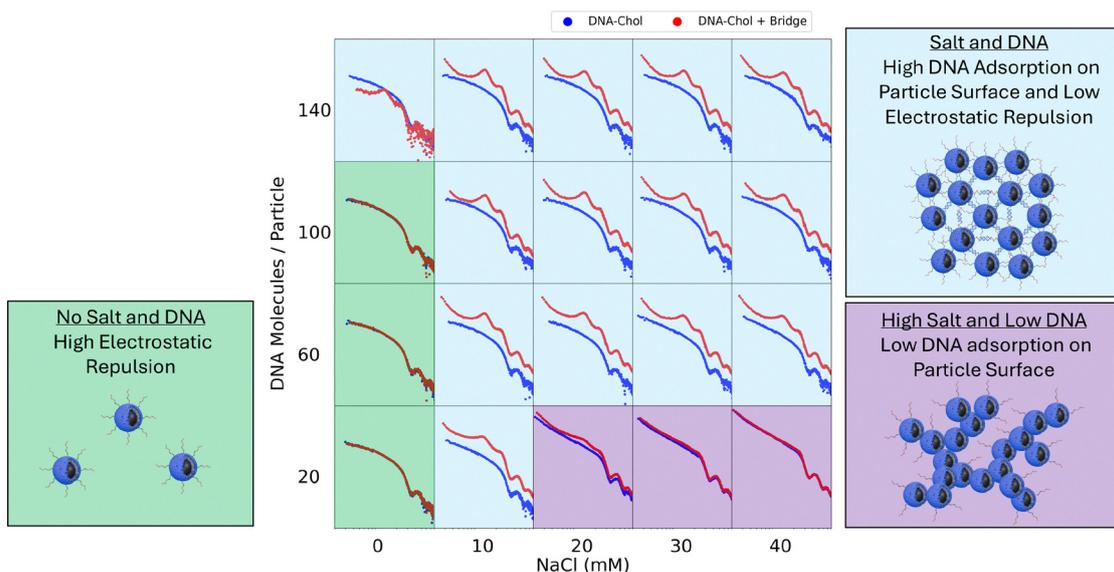
Fig. 5 The SAXS curves from the high-throughput assembly screening without any heating. The curves in blue represent the samples that do not contain DNA-Bridge, while the curves in red contain DNA-Bridge. Regions in the experimental design space that have similar SAXS curves were manually identified and highlighted with the colors green, purple, and light blue. The DNA-Bridge molecule has a length of 20 double stranded base pairs plus two single stranded 'sticky ends' of 18 base pairs on each end of the molecule.

noteworthy that in the sample prepared with 140 DNA–Chol molecules per particle at 0 mM NaCl, DNA mediated assembly is observed in the SAXS profile upon addition of DNA-Bridge. This indicates that some DNA–Chol adsorption onto the particle surface occurs even in the absence of added salt. These results suggest that the grafting density of DNA–Chol on the particle surface is directly proportional to its concentration in solution, with the proportionality influenced by the solution's ionic strength. Therefore, while NaCl is not strictly required for DNA–Chol adsorption, it enhances the efficiency of grafting, likely by mitigating electrostatic repulsion between the negatively charged DNA strands or between the strands and the particle surface.

In the purple region of Fig. 5, the SAXS curves exhibit a steep power-law decay, indicative of large, aggregated structures. Similar to the green region, the addition of DNA-Bridge does not lead to significant structural changes. This regime corresponds to conditions of low DNA–Chol density per particle combined with high NaCl concentration. We hypothesize that insufficient surface coverage by DNA–Chol prevents effective steric stabilization, resulting in dense aggregation prior to the introduction of DNA-Bridge. In contrast, the light blue region features a pronounced scattering peak near 0.0136 Å^{-1}, consistent with an interparticle spacing that arises due to the length of DNA linking the particles. In this case, the SAXS curves differ notably upon addition of DNA-Bridge, supporting
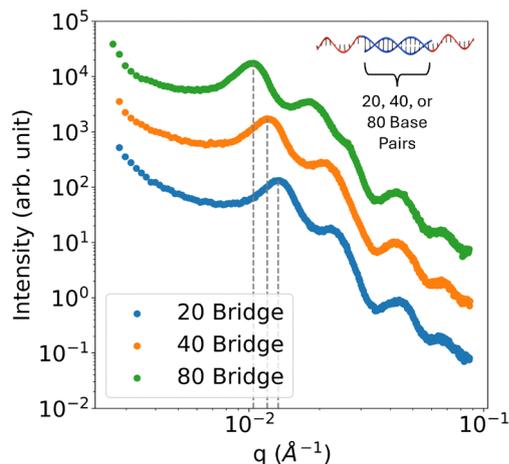
Fig. 6 SAXS intensity data showing the effect of different DNA-Bridge lengths on the assembly without any thermal annealing protocol. All DNA-Bridge molecules have the same base pairs on the ends of the molecule, but different in the amount of base pairs in the center. These samples were made with 10 mM NaCl and 100 DNA molecules/particle but with DNA-Bridge molecules of varying lengths.

the conclusion that DNA-Bridge actively drives the formation of linked particle assemblies. Despite this, it is clear that the assembly is not completely crystalline because of the relatively broad peak and the absence of additional peaks, which are characteristic of crystal structures. We would also like to point out that there is evidence that we are likely saturating the particle surface with DNA–Chol molecules when we add 100 DNA Molecules/particle. In Fig. 5, there is not much difference between the SAXS curves of samples with 100 and 140 DNA molecules/particle. This indicates that the particle surface could be fully saturated with DNA.

If the DNA-Bridge is indeed responsible for inducing assembly, then varying the length of the DNA-Bridge should result in assemblies of different interparticle spacings, which would result in SAXS curves with peaks in different locations. This hypothesis was tested by using modified DNA-Bridge molecules that have the same sequence on their complementary 'sticky ends', but a higher number of base pairs in the section of the bridge that does not interact with DNA–Chol. The results of this experiment are shown in Fig. 6, where the increase in DNA-Bridge length clearly shows the peak positions shift to a lower q, indicating a longer interparticle spacing.

One possibility is that some lipid bilayers may encapsulate more than one particle, and that this could lead to correlations between particles. Although we expect this would be rare, we cannot fully exclude the possibility of multiple particles being encapsulated by a lipid layer. Still, control experiments performed in the absence of DNA-Bridge conclusively demonstrate that no assembly is observed. Thus, cluster formation does not occur *via* lipid encapsulation alone and it is only possible when DNA is both available in the lipid covered particles and when the DNA-Bridge is added.

SAXS analysis

To analyze the experimental SAXS data shown in Fig. 5, a fitting algorithm that combines Bayesian optimization with molecular

simulations was used and is shown in Fig. 7. This approach is inspired by inverse design strategies, where interaction potentials are discovered by matching simulated structures to a desired target.[31] In these simulations, an ultra-coarse-grained model in HOOMD was used, where each silica nanoparticle of diameter $\sigma = 1$ is represented by a single point, and interparticle interactions are implemented using the modified Lennard-Jones potential (1) described in Mao *et al.*[16] In that work, the potential was validated by a more realistic simulation of the assembly of DNA-coated particles. The modified Lennard-Jones potential is defined by four parameters which were optimized using the algorithm, U_0 (optimization range of 0–150), which controls the depth of the potential, r_0, which is the distance where the interparticle interaction is minimum, and n (1–30) and m (1–30), which control the shape and sharpness of the potential. The range of r_0 was set to approximately match the calculated interparticle spacing of the particles based on the length of DNA-Bridge. In addition, the number density of particles (0.0005–0.05) in units of particles/σ^3 inside the simulation box was also added to control the aggregation kinetics and the resulting structure of the final assembly. The Bayesian optimization algorithm was free to suggest combinations of these parameters within the specified ranges, which were then used to perform the molecular simulation. To capture the system at a state close to equilibrium, SAXS curves were simulated for six frames that were spaced apart by 50 000 timesteps near the end of the simulation using an efficient Monte Carlo method,[17] and averaged to generate a representative scattering profile. The potential energy of the system was plotted for each simulation to verify that the simulation time was enough for the system to achieve a state close to equilibrium. The structure factor was then calculated from the scattering profile and then compared to the corresponding experimental structure factor using a geometry-based similarity metric.[18] The resulting similarity score was then fed back into the optimization algorithm, which iteratively refined the parameters over multiple rounds. It is important to acknowledge the limitations of using simulations to fit experimental scattering data. One limitation is that the optimal parameters are not unique, meaning that several combinations of simulation parameters could give similar results. Another is that the simulation parameters (*e.g.*, U_0, m, and n) are not directly translatable to physical experimental variables such as DNA concentration or the number of hybridizable sticky ends. Addressing these limitations would require more detailed and expensive simulations that consider the effect of DNA sequence and concentration on the interparticle potential. Nevertheless, we find this approach to be essential to capture the complexity of the dispersed semi-crystalline assembled structures that are observed in SAXS, which cannot be properly represented by analytical scattering models.

The optimization results are presented in Fig. 8(A) with reasonable agreement between the simulated and experimental structure factors. Simulation snapshots of the structure of the particles are shown in Fig. 9. The good match between the structure factors at low-q ($\leq 10^{-2}$ Å^{-1}) for the samples with
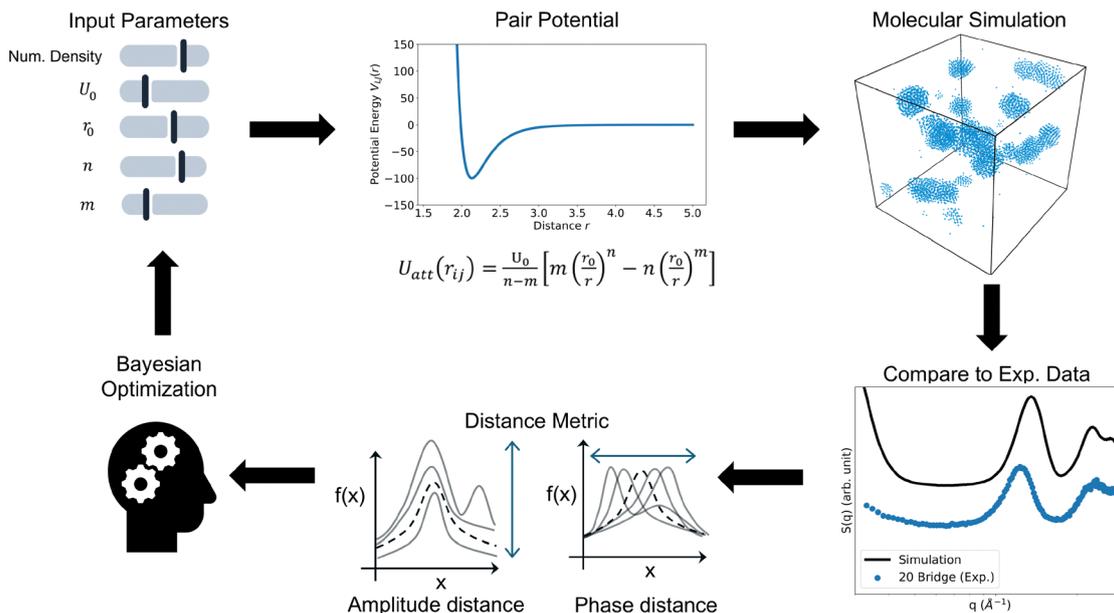
Fig. 7 The optimization protocol used to match the simulated SAXS curve from a molecular simulation to the experimental curve. The optimal input parameters that define the pair potential as well as the molecular simulation are determined by Bayesian optimization.
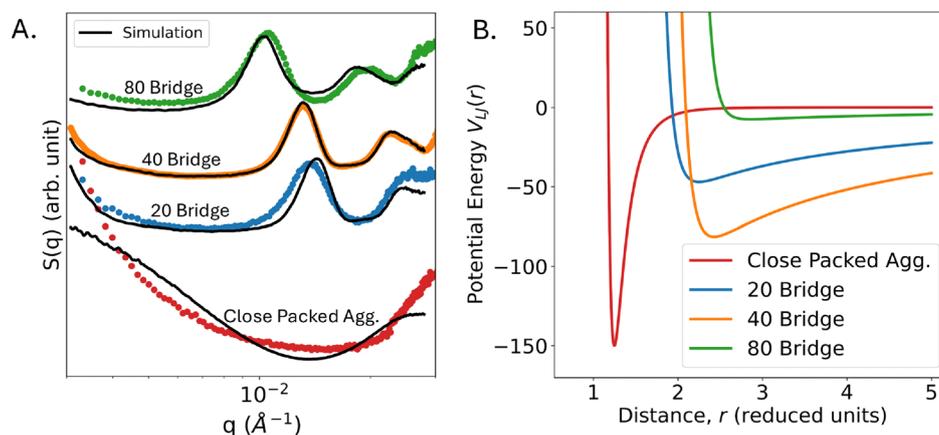
The equation shown in Fig. 7:

$$U_{att}(r_{ij}) = \frac{U_0}{n-m}\left[m\left(\frac{r_0}{r}\right)^n - n\left(\frac{r_0}{r}\right)^m \right]$$

Fig. 8 (A) The results of four independent optimization campaigns are shown as simulated structure factors plotted with the targeted experimental ones. The curves are manually shifted in intensity for visualization purposes. (B) Shows the optimized interparticle potentials used to run the simulations. The unit of the potential energy is in kT. The units of the distance are in reduced units where one reduced unit is equal to the diameter of the silica nanoparticle (25 nm).

DNA-Bridge suggests that the cluster size from the simulations match the experiments. Using the cluster analysis tool from the OVITO software[32] with a cut off distance of 3.5, the average spherical cluster diameter from the molecular simulations were determined to be 824 ($\pm$) 324 nm for 20 Bridge, 1392 ($\pm$) 646 nm for 40 Bridge, and 2282 ($\pm$) 648 nm for 80 Bridge. It is difficult to experimentally verify the cluster size, due to sedimentation effects. However, in Fig. 11(F), the average size of the cluster of the sample with 20 Bridge determined by DLS is around 600 nm which is close to the size of 824 ($\pm$) 324 nm determined from the simulation. At mid-q ($\geq 10^{-2}$ Å^{-1}), the agreement between the correlation peaks suggests that the structures from the molecular simulations are also consistent

with the interparticle spacing within the clusters, as well as the relative arrangement of the particles in the experiments. The optimized simulation parameters, including the interparticle distance, are shown in Table 1. The values for the interparticle distance can be compared to calculated values, since the length of the silica nanoparticle, lipid bilayer, and DNA are known. The length of a DNA base pair is known to be 0.34 nm per base pair,[33] and the DNA sequences of the samples can be found in the SI. The lipid bilayer thickness is about 3.6 nm from SANS data shown in Fig. 3, and the silica particle diameter is 25 nm from SAXS data. Using all this information, the interparticle distance of 20 Bridge should be 58.2 nm, 40 Bridge should be 65.2 nm and 80 Bridge should be 79.2 nm. These values are
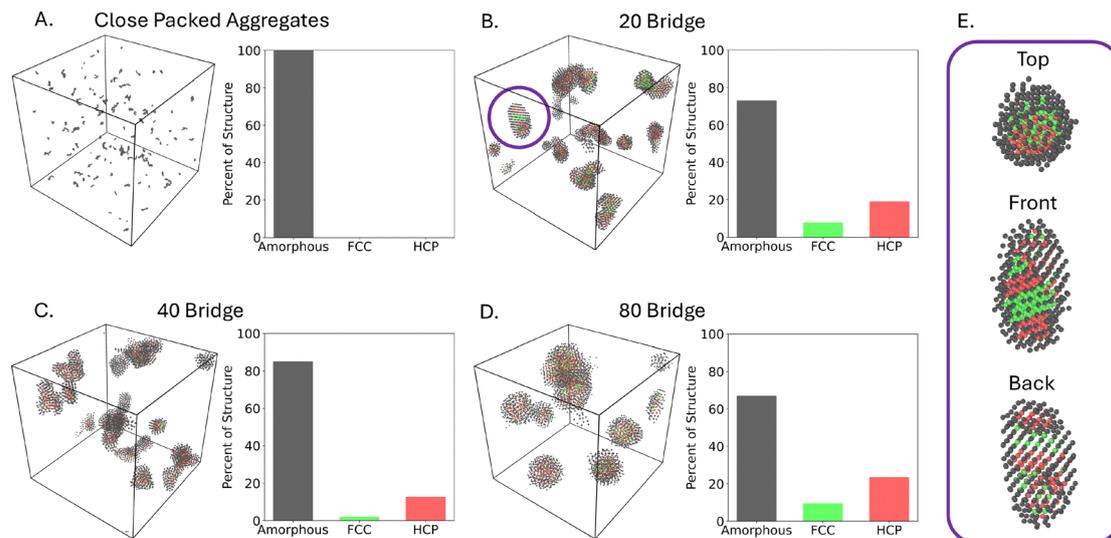
Fig. 9 (A)–(D) Crystallinity analysis on the final snapshot of the simulation for each of the samples. The polyhedral template method[34] categorizes each particle into known structures (amorphous, FCC, HCP) according to the topology of the local environment. (E) A zoomed in view of the top, front, and back of the cluster circled in purple.

Table 1 Optimal simulation parameters found by fitting structure factors derived from molecular simulations to experimental ones. U_0 has units of kT. The number density has units of particles/σ^3, where σ is the size of one particle. r_0, the interparticle distance, is reported in units of σ as well as the actual length in nm

Sample	Num. density	U_0	r_0	n	m
Close Packed Agg.	0.0005	150	1.24 (32 nm)	8.41	28.92
20 Bridge	0.0050	46.95	2.25 (59 nm)	1.00	20.89
40 Bridge	0.0050	81.42	2.42 (63 nm)	1.00	21.78
80 Bridge	0.0050	7.46	2.86 (74 nm)	1.00	30.00

close to the interparticle distances in Table 1, suggesting a reasonable fit. There is a small disagreement between the interparticle spacing as the length of the bridge gets longer. This could be explained by the increased flexibility of longer DNA bridge strands, which may cause the actual distance to be shorter than the expected one. Although the 'best' fit for the example close-packed aggregate sample was not ideal, the interparticle spacing of 32 nm from the simulations is close to the expected spacing between silica nanoparticles encapsulated in a liposome, which was calculated to be 32.2 nm.

The final kinetically stable structures from the molecular simulations can be further analyzed to determine the degree of crystallinity in the structures. The polyhedral template method[34] in OVITO was used to do this. This method classifies particles into categories according to the topology of the local environment, and is a robust method for structures that are not completely crystalline. The results of the analysis are shown in Fig. 9, where the percent of particles categorized in each structure are shown in a bar plot. From the figure, it is clear that DNA induces the assembly of the particles into semi-crystalline composite structures of HCP and FCC ($\sim$30%) and amorphous arrangements of primary particles. For all samples, most primary particles ($\geq$60%) are found in amorphous

regions, which is consistent with the relatively broad peak observed in the structure factors and the absence of higher-order reflections. By visualizing a single cluster, shown in Fig. 9(E), it was observed that the crystalline regions are located in the center of the cluster, while the amorphous regions are located on the surface of the clusters. Electron microscopy was performed of the 20 Bridge sample and the images are shown in Fig. 10. In the images, there are many dense regions which we hypothesize to be the particles with crystalline arrangements, while the lighter regions contain particles with amorphous ones. Based on these results, we hypothesize that one way to increase the crystallinity of the sample is to increase the cluster size, which would maximize the crystalline regions. Drying effects due to processing for electron microscopy can have a significant effect on our system by inducing aggregation of the clusters, resulting in the observation of larger domains in the images. Our system is also mainly controlled by hydrophobic interactions (lipid–lipid, DNA–lipid) that are very sensitive to drying effects. Free particles, lipid, or DNA in the sample could also further aggregate during drying, making the clusters larger that they were in the dispersed state. In Fig. 10, we highlight that dense darker regions in the clusters can be evidence for smaller crystalline regions observed in simulations, while the lighter regions are likely amorphous. It is hard to draw quantitative conclusions from the size of the aggregates in the images due to the influence of drying effects.

According to these results, crystalline structures can be achieved without a thermal annealing protocol by using physically tethered DNA bonds on the nanoparticle surface. This could suggest that the mobility of the tethers enables particles to reconfigure and rearrange into ordered arrangements. This behavior stands in contrast to the more common approach of using immobile gold–thiol bonds to attach DNA molecules to nanoparticle surfaces, where crystallinity cannot be obtained
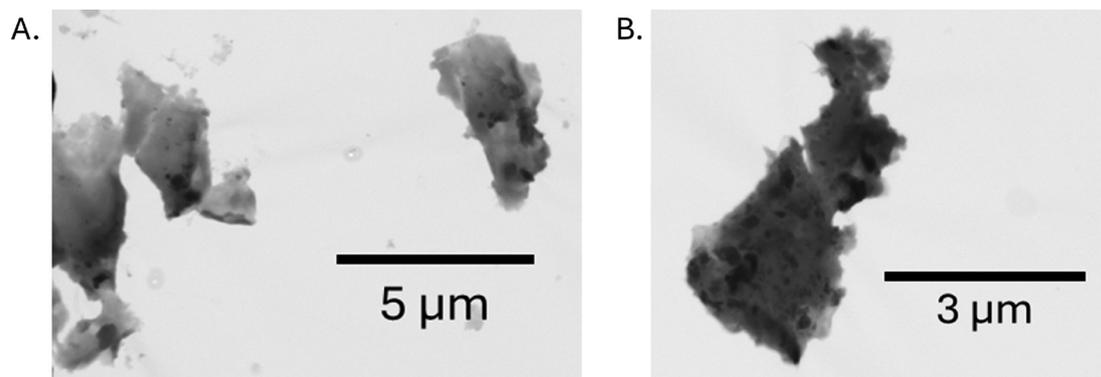
Fig. 10 Electron microscopy images of the 20 Bridge sample taken roughly 24 hours after assembly was initialized. The sample was diluted by a factor of 100 and then dried on a microscopy grid. The parameters for (A) are: Mag. 22 000×, FW 23.7 µm, HV 15 kV, Int. Map, Det. STEM, WD 8.091 mm. The parameters for (B) are: Mag. 42 000×, FW 12.3 µm, HV 15 kV, Int. Map, Det. STEM, WD 7.896 mm.

without a thermal annealing step.[3,35] Although we have not yet achieved the well-defined crystal superlattices reported in other systems, we believe that increasing the cluster sizes in our system could make this potentially possible.

The SAXS analysis presented in this section also demonstrates that efficient particle dynamics simulations can be used to directly fit SAXS data by automatically tuning simulation parameters, such as the interparticle potential and particle number density, within a closed-loop optimization framework. With this method, a simulation file containing the positions of each particle at a state close to equilibrium can be obtained and further analyzed for cluster size and crystallinity. This approach is valuable because it allows for the influence of various experimental design parameters (e.g., particle shape, particle size, DNA length) on the final assembly to be evaluated in silico

before conducting the experiment. For example, simulations can aid in designing large crystalline assemblies with targeted symmetries (e.g., FCC, BCC) by first identifying, through parameter sweeps, the trends that promote their formation. This information can then be applied to the experimental setup.

Assembly kinetics and mechanism

The mechanism at which the particles assemble was investigated using time resolved SAXS and DLS. The sample containing 1 mg mL^{-1} silica encapsulated in DOPC, 10 mM NaCl, and 100 DNA Molecules/Particle and the DNA-Bridge with 20 base pairs was recreated and characterized at approximately every 10 minutes after inducing assembly. The results of the experiment are shown in Fig. 11. From Fig. 11(A) the peak corresponding to the interparticle spacing at around 0.0136 Å^{-1} is
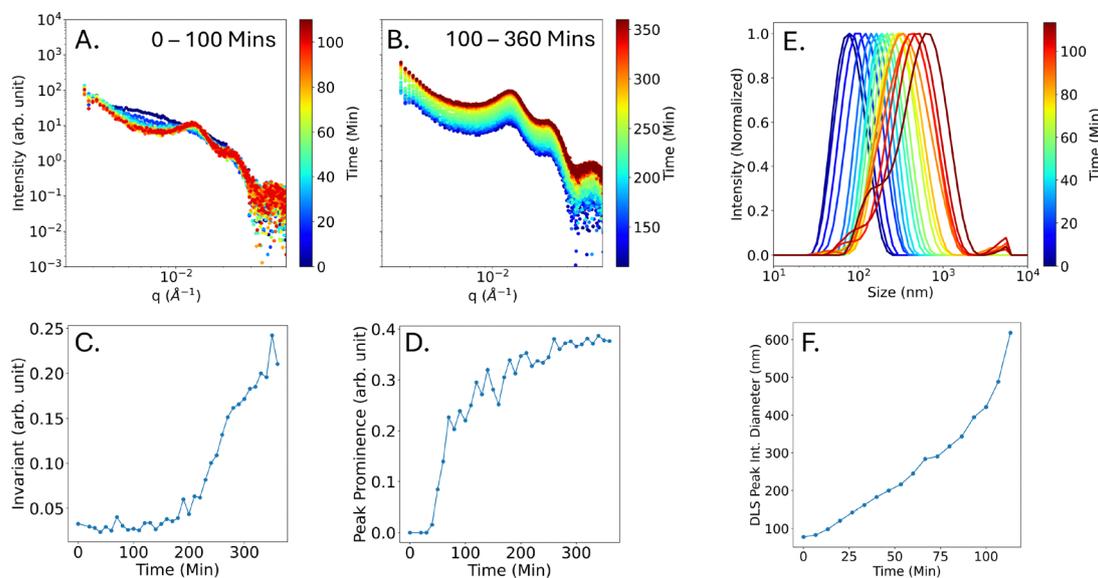

Fig. 11 Time resolved SAXS and DLS measurements of the sample 20 Bridge. The initial time (t = 0) corresponds to the time at which the DNA–Bridge was added to the sample. (A) Shows the SAXS curves of the first 100 minutes. (B) Shows the SAXS curves of minute 100 to 360. (C) Shows the invariant of all the SAXS curves as a function of time. (D) Shows the peak prominence of the SAXS curves, which was determined by the height of the peak minus the trough. (E) Shows the results from DLS of the first 100 minutes of assembly. (F) Is derived from the DLS data and shows the location of the peak position as a function of time.
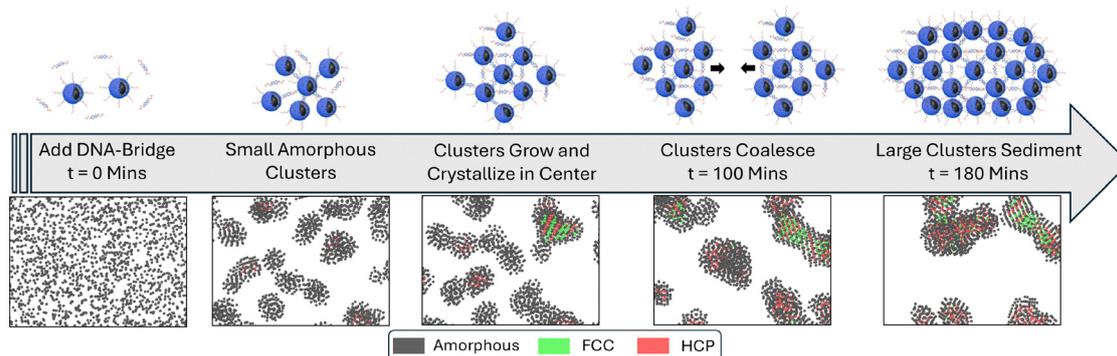
Fig. 12 The proposed mechanism of the assembly of the DNA coated DOPC encapsulated silica nanoparticles. The timesteps in the figure are based on the interpretation of experimental SAXS and DLS data. The mechanism is consistent with simulation snapshots of the sample with 20 Bridge.

observed to form and dramatically increase in peak prominence in the first 100 minutes. Fig. 11(B) shows the SAXS curves from minute 100 to 360. These curves mostly have the same shape, but only increase in intensity, which is a sign of sedimentation. The invariant of all the SAXS curves is plotted in Fig. 11(C). The invariant is calculated from the area under the curve and is proportional to the number of scattering objects in the beam path. From the data, the invariant stays relatively constant until 180 minutes when it starts to increase, which is evidence of the formation of assemblies that are large enough to sediment due to gravity. Fig. 11(D) shows the peak prominence of the SAXS curves as a function of time. The prominence is calculated by subtracting the intensity at the peak from the intensity at the trough. Therefore, it is insensitive to sedimentation and should represent the amount of material in the particle assemblies that have an ordered spacing. The data shows that after around 30 minutes, the peak prominence dramatically increases until about 200 minutes when it finally converges to a single value. This indicates that the assembly process is complete by this time and that the assemblies do not increase in size. In addition to SAXS, DLS was also used to characterize the sample. Fig. 11(E) shows the intensity distribution of the sample which is related to the size of objects in it. We note that DLS is only meaningful when there is random diffusion of particle suspensions. Therefore, DLS was only collected and interpreted over shorter time scales (up to 120 min) before the onset of sedimentation of larger clusters (>180 min). Fig. 11(F) was created by extracting the peak positions of the intensity distribution to track the size of the assembly as a function of time. The data shows that the assembly process takes around 10 minutes to start, but after this, the size of the assembly rapidly grows until it reaches a large size.

Together, the data from SAXS and DLS suggest that the assembly follows a classical nucleation and growth mechanism. Initially, small clusters form, and once they reach a critical size, further growth becomes thermodynamically favorable.[36] This is reflected in the SAXS data, where a correlation peak appears early during assembly and gradually increases in prominence, indicating the development of ordered structures.[37] DLS data

further support this mechanism, showing a progressive increase in the size of the assemblies over time. Eventually, we hypothesize that the clusters coalesce, making them large enough to undergo sedimentation. This mechanism is consistent with the structures in the particle simulations as shown in Fig. 12.

Conclusion

This study demonstrates the behavior of DNA-mediated assembly of lipid encapsulated silica nanoparticles. After verifying that the silica nanoparticles were properly encapsulated using a combination of scattering techniques, a high-throughput platform was used to test the effect of NaCl and DNA concentration on the assembly. The results show that while NaCl is not strictly required for DNA–Chol adsorption on the surface of the particle, it enhances the efficiency of grafting, likely by mitigating electrostatic repulsion between the negatively charged DNA–Chol strands and the particle surface. DNA–Chol strands anchored to the particle surface provide steric stabilization, and allows for controlled assembly of the nanoparticles due to the hybridization between DNA–Chol strands and DNA-Bridge strands. The resulting structures exhibit well-defined interparticle spacing that is determined by the grafted strands and the length of the DNA-Bridge. Molecular simulations combined with Bayesian optimization are used to fit the experimental structure factors and optimal simulation parameters are obtained. The resulting particle configurations reveal structural arrangements consistent with the expected interparticle distances derived from the length of DNA linking the particles. Crystallinity analysis reveals that around 30% of all particles in the sample are in a crystalline arrangement. Furthermore, the crystalline particles are located in the center of the cluster of particles while the surface of the cluster is amorphous. The ability to form crystalline structures without any thermal annealing could be due to the azimuthal mobility of DNA on the surface of the nanoparticles, but further experiments are needed to validate this. Finally, time resolved SAXS and DLS measurements are used to monitor the assembly process.

Together, the data suggests that the assembly follows a classical nucleation and growth mechanism, where small clusters form and slowly increase in size, until they coalesce and undergo sedimentation.

Author contributions

All the authors contributed equally to conceptualization and problem formulation. H. T. C. developed the experimental pipeline, wrote code for high-throughput experimentation, and particle simulations. H.Z and Z.S performed the particle simulations. N.K and H.T.C. contributed equally in experimental data collection. Z.R.W and A.M contributed to microscopy data acquisition. L.D.P, O.G., A.F, and Z.S contributed to funding acquisition.

Conflicts of interest

A.L.F is a co-founder and consultant of Evozyne, Inc. and a co-author of US Patent Applications 16/887,710 and 17/642,582, US Provisional Patent Applications 62/853,919, 62/900,420, 63/314,898, 63/479,378, 63/521,617, and, 63/669,836, and International Patent Applications PCT/US2020/035206, PCT/US2020/050466, and PCT/US24/10805.

Data availability

Data for this article, including characterization data and simulation files are available on Github (**https://github.com/pozzo-research-group/silica_lipid_DNA**).

SI includes DNA sequences, calculated scattering length densities, as well as additional data and simulations. See DOI: **https://doi.org/10.1039/d5sm00924c**.

Acknowledgements

References

1 S. Yadav Schmid, K. Lachowski, H. Thart Chiang, L. Pozzo, J. De Yoreo and S. Zhang, Mechanisms of biomolecular self-assembly investigated through in situ observations of structures and dynamics, *Angew. Chem., Int. Ed.*, 2023, **62**(48), e202309725.

2 J. S. Kahn and O. Gang, Designer nanomaterials through programmable assembly, *Angew. Chem., Int. Ed.*, 2022, **61**(3), e202105678.

3 D. Nykypanchuk, M. M. Maye, D. van der Lelie and O. Gang, DNA-guided crystallization of colloidal nanoparticles, *Nature*, 2008, **451**(7178), 549–552.

4 R. J. Macfarlane, R. V. Thaner, K. A. Brown, J. Zhang, B. Lee, S. T. Nguyen and C. A. Mirkin, Importance of the DNA ''bond'' in programmable nanoparticle crystallization, *Proc. Natl. Acad. Sci. U. S. A.*, 2014, **111**(42), 14995–15000.

5 M. Rinaldin, R. W. Verweij, I. Chakraborty and D. J. Kraft, Colloid supported lipid bilayers for self-assembly, *Soft Matter*, 2019, **15**(6), 1345–1360.

6 I. Chakraborty, D. J. G. Pearce, R. W. Verweij, S. C. Matysik, L. Giomi and D. J. Kraft, Self-Assembly Dynamics of Reconfigurable Colloidal Molecules, *ACS Nano*, 2022, **16**(2), 2471–2480.

7 A. McMullen, M. Muñoz Basagoiti, Z. Zeravcic and J. Brujic, Self-assembly of emulsion droplets through programmable folding, *Nature*, 2022, **610**(7932), 502–506.

8 M. R. Jones, R. J. Macfarlane, B. Lee, J. Zhang, K. L. Young, A. J. Senesi and C. A. Mirkin, DNA-nanoparticle superlattices formed from anisotropic building blocks, *Nat. Mater.*, 2010, **9**(11), 913–917.

9 J. S. Kahn, B. Minevich and O. Gang, Three-dimensional dna-programmable nanoparticle superlattices, *Curr. Opin. Biotechnol.*, 2020, **63**, 142–150.

10 D. Ortiz, K. L. Kohlstedt, T. Dac Nguyen and S. C. Glotzer, Self-assembly of reconfigurable colloidal molecules, *Soft Matter*, 2014, **10**, 3541–3552.

11 K. Su Khin Zaw, C. Ma, M. L. Shofner and S. Nair, Quantitative microstructure-permeation relations in graphene oxide membranes: Effects of nanosheet size on molecular weight cut-off and fractionation of complex biomass feedstocks, *J. Membr. Sci.*, 2025, **734**, 124421.

12 K. Su Khin Zaw, C. Ma, Z. Wang, M. L. Shofner and S. Nair, Effects of graphene oxide membrane thickness reduction on microstructure and crossflow separation performance in kraft black liquor dewatering, *Chem. Eng. Sci.*, 2023, **281**, 119194.

13 B. N. Khlebtsov, V. A. Khanadeev and N. G. Khlebtsov, Determination of the size, concentration, and refractive

index of silica nanoparticles from turbidity spectra, *Langmuir*, 2008, **24**(16), 8964–8970PMID: 18590302.

14 A. Gadomski, N. Kruszewska and J. M. Rubi, Derivation of the refractive index of lipid monolayers at an air-water interface, *Opt. Mater.*, 2019, **93**, 1–5.

15 J. A. Anderson, J. Glaser and S. C. Glotzer, Hoomd-blue: a python package for high-performance molecular dynamics and hard particle monte carlo simulations, *Comput. Mater. Sci.*, 2020, **173**, 109363.

16 R. Mao, B. Minevich, D. McKeen, Q. Chen, F. Lu, O. Gang and J. Mittal, Regulating phase behavior of nanoparticle assemblies through engineering of dna-mediated isotropic interactions, *Proc. Natl. Acad. Sci. U. S. A.*, 2023, **120**(52), e2302037120.

17 H. Thart Chiang, Z. Zhang, K. Vaddi, F. Akif Tezcan and L. D. Pozzo, Efficient analysis of small-angle scattering curves for large biomolecular assemblies using Monte Carlo methods, *J. Appl. Crystallogr.*, 2025, **58**(3), 963–975.

18 V. Kiran, C. Huat Thart and D. Pozzo Lilo, Autonomous retrosynthesis of gold nanoparticles via spectral shape matching, *Digital Discovery*, 2022, **1**, 502–510.

19 M. Balandat, B. Karrer, D. R. Jiang, S. Daulton, B. Letham, A. Gordon Wilson and E. Bakshy, BoTorch: A Framework for Efficient Monte-Carlo Bayesian Optimization, *Advances in Neural Information Processing Systems*, 2020, **33**.

20 Y. Han, Z. Lu, Z. Teng, J. Liang, Z. Guo, D. Wang, M.-Y. Han and W. Yang, Unraveling the growth mechanism of silica particles in the stöber method: In situ seeded growth model, *Langmuir*, 2017, **33**(23), 5879–5890PMID: 28514596.

21 J. Kobierski, A. Wnetrzak, A. Chachaj-Brekiesz and P. Dynarowicz-Latka, Predicting the packing parameter for lipids in monolayers with the use of molecular dynamics, *Colloids Surf., B*, 2022, **211**, 112298.

22 J. Liu, Interfacing Zwitterionic Liposomes with Inorganic Nanomaterials: Surface Forces, Membrane Integrity, and Applications, *Langmuir*, 2016, **32**(18), 4393–4404.

23 H. Wang, J. Drazenovic, Z. Luo, J. Zhang, H. Zhou and S. L. Wunder, Mechanism of supported bilayer formation of zwitterionic lipids on SiO_2 nanoparticles and structure of the stable colloids, *RSC Adv.*, 2012, **2**(30), 11336.

24 S. Ahmed and S. L. Wunder, Effect of High Surface Curvature on the Main Phase Transition of Supported Phospholipid Bilayers on SiO_2 Nanoparticles, *Langmuir*, 2009, **25**(6), 3682–3691.

25 H. I. Alkhammash, N. Li, R. Berthier and M. R. R. De Planque, Native silica nanoparticles are powerful membrane disruptors, *Phys. Chem. Chem. Phys.*, 2015, **17**(24), 15547–15560.

26 M. Elizabeth Beattie, S. L. Veatch, B. L. Stottrup and S. L. Keller, Sterol structure determines miscibility versus melting transitions in lipid vesicles, *Biophys. J.*, 2005, **89**(3), 1760–1768.

27 M. Ju Shon, S.-H. Rah and T.-Y. Yoon, Submicrometer elasticity of double-stranded dna revealed by precision force-extension measurements with magnetic tweezers, *Sci. Adv.*, 2019, **5**(6), eaav1697.

28 H. Thart Chiang, K. Vaddi and L. Pozzo, Data-driven exploration of silver nanoplate formation in multidimensional chemical design spaces, *Digital Discovery*, 2024, **3**, 2252–2264.

29 N. Paracini, P. Gutfreund, R. Welbourn, J. Francisco Gonzalez-Martinez, K. Zhu, Y. Miao, N. Yepuri, T. A. Darwish, C. Garvey, S. Waldie, J. Larsson, M. Wolff and M. Cárdenas, Structural characterization of nanoparticle-supported lipid bilayer arrays by grazing incidence x-ray and neutron scattering, *ACS Appl. Mater. Interfaces*, 2023, **15**(3), 3772–3780PMID: 36625710.

30 H. D. Hill, J. E. Millstone, M. J. Banholzer and C. A. Mirkin, The Role Radius of Curvature Plays in Thiolated Oligonucleotide Loading on Gold Nanoparticles, *ACS Nano*, 2009, **3**(2), 418–424.

31 B. A. Lindquist, Inverse design of equilibrium cluster fluids applied to a physically informed model, *J. Chem. Phys.*, 2021, **154**(17), 174907.

32 A. Stukowski, Visualization and analysis of atomistic simulation data with OVITO-the Open Visualization Tool, *Modell. Simul. Mater. Sci. Eng.*, 2010, **18**(1), 015012.

33 J. D. Le, Y. Pinto, N. C. Seeman, K. Musier-Forsyth, T. Andrew Taton and R. A. Kiehl, Dna-templated self-assembly of metallic nanocomponent arrays on a surface, *Nano Lett.*, 2004, **4**(12), 2343–2347.

34 P. Mahler Larsen, S. Schmidt and J. Schiøtz, Robust structural identification via polyhedral template matching, *Modell. Simul. Mater. Sci. Eng.*, 2016, **24**(5), 055007.

35 R. J. Macfarlane, M. R. Jones, A. J. Senesi, K. L. Young, B. Lee, J. Wu and C. A. Mirkin, Establishing the design rules for dna-mediated programmable colloidal crystallization, *Angew. Chem., Int. Ed.*, 2010, **49**(27), 4589–4592.

36 S. Karthika, T. K. Radhakrishnan and P. Kalaichelvi, A review of classical and nonclassical nucleation theories, *Cryst. Growth Des.*, 2016, **16**(11), 6663–6681.

37 S. Wang, A. Favor, R. Daniel Kibler, J. Morris Lubner, A. J. Borst, N. Coudray, R. Redler, H. Thart Chiang, W. Sheffler, Y. Hsia, Z. Li, D. Charles Ekiert, G. Bhabha, L. D. Pozzo and D. Baker, Bond-centric modular design of protein assemblies, *Nat. Mater.*, 2025, 1–9.